Microfluid Nanofluid (2017) 21:146
DOI 10.1007/s10404-017-1986-4

RESEARCH PAPER

On the thin-film-dominated passing pressure of cancer cell squeezing through a microfluidic CTC chip

Xiaolong Zhang[1] · **Xiaolin Chen**[1] · **Hua Tan**[1]

Received: 31 January 2017 / Accepted: 10 August 2017 / Published online: 18 August 2017

Abstract Detection of circulating tumor cells (CTCs) shows strong promise for early cancer diagnosis, and cell-deformation-based microfluidic CTC chips have been playing an important role. For the design and optimization of high-throughput CTC chips, the dynamic pressure drop in the microfluidic chip during the CTC passing process is a key parameter related to the device sensitivity and filtering performance and has to be given very serious consideration. Although insights have been provided by previous researches, there is still a lack of understanding of the fundamental physics and complex interplay between viscous tumor cell and the flow inside the microfluidic filtering channel. In this paper, the process of the viscous cell squeezing through a microchannel is modeled by solving the governing equations of microscopic multiphase flows, with the tumor cell modeled by a droplet model and the immiscible cell–blood interface tracked by the volume-of-fluid method. Detailed dynamics regarding the filtering process is discussed, including the cell deformation, flow characteristics, passing pressure characteristics as well as the relationship between the pressure drop across the device and the thin film formed in the filtration channel. Current simulation shows a good agreement with analytic results, and an analytical formula is proposed to predict the passing pressure in the microchannel. Our study provides insights into the fluid physics of a viscous cell passing through a constricted microchannel, and the proposed formula can be readily applied to the design and optimization of cell-deformation-based microchannels for CTC detection.

✉ Xiaolin Chen
chenx@wsu.edu

[1] Mechanical Engineering Program, Washington State University, Vancouver, WA 98686, USA

Keywords Cancer diagnosis · CTC detection · Passing pressure · Thin film · Microfluidic chips · Design and optimization

1 Introduction

As a leading cause of death worldwide, cancer is increasingly a global health issue. Over 20% of deaths are caused by cancer and over 8 million people die of cancer each year throughout the world (Torre et al. 2015). The mortality rate of cancer is mainly due to metastasis, which accounts for 90% of human death (Weigelt et al. 2005). Metastasis is the spread of cancer from one organ to another. It occurs when some cancer cells break away from the primary tumor and travel through the blood system to form new tumors at a distant site (Gupta and Massagué 2006). These cancer cells, present in the blood stream and capable of metastasis, are termed circulating tumor cells (CTCs). CTCs have been increasingly recognized as a potential biomarker for early cancer detection due to their key role in metastasis initiation (Krebs et al. 2010). However, enrichment and investigation of CTCs have been extremely difficult due to the extreme rarity of CTCs in blood. Detecting and separating CTCs are like finding the needle in a haystack, as they are at a concentration of 1 CTC in 1 ml blood, and the ratios of CTCs to red blood cells (RBDs) and white blood cells (WBDs) are ~$1/10^9$ and ~$1/10^7$, respectively (Jin et al. 2014).

Various experimental methods for CTC detection and separation have been proposed (Bonner et al. 1972; Di Carlo 2009; Ding et al. 2013; Fulwyler 1965; Gascoyne et al. 2009; Huang et al. 2004; Melville et al. 1975; Miltenyi et al. 1990). These methods can be categorized into two types: biochemical and biophysical. Biochemical CTC detection methods are based on biomarkers and the affinity binding of the target

cell and biochemical labels. A key challenge associated with biochemical methods is that CTCs are inherently heterogeneous and do not universally express specific tumor markers (Jin et al. 2014). CTCs may also escape from biochemical detection due to their loss of expression for the specific adopted biochemical marker (e.g., epithelial cell adhesion molecule, EpCAM, and cytokeratins, CK) during the cell transition process (e.g., epithelial-to-mesenchymal transition, EMT; Allan and Keeney 2009; Polyak and Weinberg 2009). Besides, there is a possibility that other undesired cells may also express similar biomarkers like the CTCs, thus contaminating the CTCs enrichment and compromising the separation accuracy (Sieuwerts et al. 2009). Moreover, the biochemical labels such as fluorophore or microbeads may lead to cytotoxicity, which can affect the cell function and viability as well as the following biological study of CTCs (Kumar and Bhardwaj 2008; Münz et al. 2010; Warkiani et al. 2016).

The persistent challenges in biochemical methods encourage the research on biophysical methods, which demonstrate the potential to address some of the problems in biochemical methods (Cima et al. 2013). Instead of using biochemical labels, biophysical methods sort CTCs based on intrinsic physical characteristics of CTCs such as cell size, deformability, and electrical polarizability. Since no labels are used in the sorting process, these label-free methods eliminate the cell-labeling process and thus require less manipulation of the cells with a much simpler procedure (Gossett et al. 2010), meanwhile reducing the cost by the elimination of biochemical labels such as microbeads and antigens (Liu et al. 2013; Shelby et al. 2004; Whitesides 2006). Also, the CTCs keep better original viability and function since they are not altered by the biochemical markers such as antigens or fluorophores (Jin et al. 2014). In addition, label-free methods are easily applicable to portable microfluidic devices in which the volume of reagent is significantly reduced. Since the pioneer work of separating cancer cells was based on pore-type structures on a plastic tape (Seal 1964), biophysical label-free methods have received intensive interest. These studies include microconfigured separators based on cell size and deformation (Seal 1964), the deterministic lateral displacement (DLD) method based on the hydrodynamic properties of cells (Huang et al. 2004), inertial focusing method based on the inertial effects (Bhagat et al. 2011), the dielectrophoresis (DEP) method based on cell polarizability properties (Gascoyne et al. 2009), and acoustophoresis based on cell acoustical properties (Ding et al. 2013; Ren et al. 2015).

As one of the label-free methods, the cell-deformation-based method has advantages such as simple structure configuration, low cost, and reliable operation performance (McFaul et al. 2012; Mohamed et al. 2009), with which various configuration structures are available including microscale confinement channel (Zhang et al. 2014c, 2015a), membranes with pores (Lu et al. 2010; Zheng et al. 2007, 2011), weir structures in a microchannel (Brody et al. 1996; Chen et al. 2008; Crowley and Pizziconi 2005; VanDelinder and Groisman 2006), funnel structures (Guo et al. 2011), and pillar structures (Jönsson et al. 2008; Mohamed et al. 2007). The cell-deformation-based method shows good isolation outcome with high preservation of cell viability for subsequent metastasis analysis and easy integration into lab-on-a-chip devices. The separation efficiencies can be up to 95 and 96% for tumor cell capture and white blood cell clearance, respectively (Ji et al. 2008; McFaul et al. 2012; Tang et al. 2014). Experimental methods have made notable contributions to the field of cell separation, while being tempered by persistent difficulties in device manufacturing, prohibitive cost of experimental systems, and complex operating of such experiments.

To address the challenges in the experimental methods, numerical simulation has been conducted to probe the fundamentals of such microfluidic devices (e.g., the characteristics of the operating pressure which drives the cell-deformation-based CTC separation system) to complement experiments (Zhang et al. 2014a, b, 2015b). Various models such as the micro-/nano-structural model (Boey et al. 1998; Freund 2014; Li et al. 2005) and the continuum model (Lim et al. 2006; Peng et al. 2013; Secomb and Hsu 1996) have been proposed for cell modeling. The micro-/nano-models consider the subcellular interactions and are often prohibitively expensive when employed in the numerical simulation. For continuum models, a solid shell (or cytoskeleton)-enclosed viscous fluid model has been widely used to model the cell behavior in the literature (Lim et al. 2006). For cells that undergo large deformation, liquid droplet models have been proposed. Although providing less insight at the subcellular level, the liquid droplet model is simple and straightforward for large cell-deformation problems which occur and dominate during the CTC passing process (Zhang et al. 2014c, 2015a). Luo et al. (2014) used a continuum solid model consisting of viscoelastic material to simulate the process of a lung tumor cell entering a microconfinement based on finite element method. The numerical simulation compared well with experimental results and demonstrated a two-stage cell entry process, which consists of a rapid jump into the constriction and a following creeping aspiration stage with increase in aspiration length caused by viscoelastic properties. Zhang et al. (2014c, 2015a) employed a continuum liquid droplet model with identical viscosity to the ambient blood plasma for cell modeling and numerically studied the squeezing process of CTCs and WBCs entering a microfiltration channel based on finite volume method (FVM). The squeezing pressure signatures of different cells at various flow rates were obtained and characterized. The concept of optimum velocity was also introduced, which is meaningful

for the cellular behavior explanation during the filtration process and provides valuable information for the design and optimization of CTC microfilters. Aghaamoo et al. (2015) investigated the cell-deformation-based tumor cell separation within conical-shaped microfilters based on the finite volume method. The tumor cell was modeled by the continuum liquid droplet model, which is assigned identical viscosity with the ambient blood plasma. Although the threshold pressure is slightly under predicted, their simulation results such as cell deformation and pressure signatures showed good agreement with experiments. Also discussed are the effects of conical-shaped geometries on the threshold pressure and cell deformation, which are useful for efficient CTC separation devices.

Despite the successful applications of the continuum models above, it is noteworthy that the high-viscosity properties of the CTCs are neglected in the numerical studies employing the liquid droplet model. In the liquid droplet model employed in these studies, the highly viscous cell is oversimplified to a liquid droplet with identical viscosity to that of the blood plasma. As a matter of fact, the viscosity can play a significant role in the dynamics of the cell in such microfluidic devices (Faivre et al. 2006; Nie et al. 2008; Xiong and Zhang 2012), and thus, a model considering the high viscosity of the cell is desired for better accuracy.

In this paper, we propose a continuum highly viscous liquid droplet model (Zhang et al. 2015a) to investigate the CTCs behavior during the microfiltration process. The continuum liquid droplet model describes a two-phase flow consisting of highly viscous Newtonian fluid. The interface is tracked by using the volume-of-fluid (VOF) model, and the surface tension is modeled by the continuum-surface-force (CSF) method. The motion, deformation, and pressure characteristics of the CTC passing through a microfilter are studied and discussed in detail. Also discussed are the effects of viscosity ratio on the cell behavior and microfiltration process. Numerical results obtained from the highly viscous droplet model are compared with analytic results regarding the cell deformation as well as flow characteristics such as velocity and pressure distributions. The dominating flow characteristics are identified. A formula for pressure drop is also proposed, which can be used for quick estimation and characterization of the pressure during the filtration process of such microfluidic devices.

2 Model description

The physical model of a cell squeezing through a microfilter is illustrated in Fig. 1. The microfilter consists of an entrance chamber, an exit chamber, and a filtration channel. The entrance and exit chambers are considered identical cylinders with a cylinder radius (r_{cham}) of 15 μm. When blood samples flow through the microfilter, the more deformable normal blood cells will squeeze through the microfilter, but the stiffer CTCs will be blocked by the system (Hur et al. 2011). The critical diameter of the filtration channel is reported to be within 5–12 μm for effective filtering of CTCs according to different cell sorting methods (Zhang et al. 2014c). The filtration channel adopted here is considered cylindrical with a radius (r_{ch}) of 4 μm.

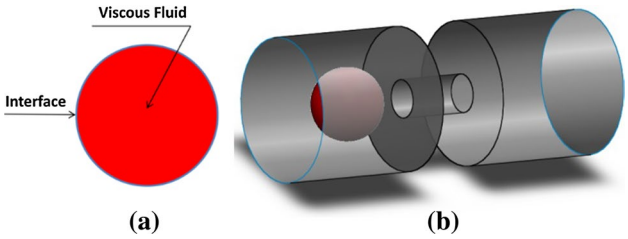

Fig. 1 Viscous cell model and microfilter configuration: **a** viscous cell, **b** microfilter

For convenience, typical CTC properties that fall within the reported range are employed in our model (Preetha et al. 2005). The CTC is modeled using a viscous droplet encapsulated by constant surface tension as shown in Fig. 1. The elastic property of a cell is taken into account by using the equivalent surface tension effect. For cervical cancer cells, the effective surface tension value is set as 50 mN/m based on previously published single cell deformability experiments (Preetha et al. 2005; Zhang et al. 2014c, 2015a). The internal cell structures (such as the DNA sequence, lipid layer, and cytoskeleton) as well as the internal flow details (such as vortex inside the cell) are neglected. The viscosity of the CTC is considered to be ranging from 0.001 to 0.064 Pa·s (Lim et al. 2006; Preetha et al. 2005). The viscosity of the blood plasma is set as a constant of 0.001 Pa·s (Leong et al. 2011; Marella and Udaykumar 2004), and all the channel walls are assumed to be non-wetting with a contact angle of 180°. Detailed filtration parameters and the CTC properties are listed in Table 1.

3 Theoretical background

In general, the flow in the microfilter is controlled by the continuity and momentum equations which are expressed as,

$$\begin{cases} \dfrac{\partial}{\partial t}(\rho) + \nabla \cdot (\rho \vec{u}) = 0 \\ \dfrac{\partial}{\partial t}(\rho \vec{u}) + \nabla \cdot (\rho \vec{u}\vec{u}) = -\nabla p + \nabla \cdot (\mu(\nabla \vec{u} + \nabla \vec{u}^{\mathrm{T}})) + \rho \vec{g} + \vec{F} \end{cases} \tag{1}$$

where ρ is fluid density, u is the flow velocity, p is the pressure, μ is the dynamic viscosity, $\vec{g}$ is gravitational

Table 1 Parameters of the cell and the microfilter

Parameters	Settings
CTC radius r_{cell} (μm)	8
Filtration channel radius r_{ch} (μm)	4
Chamber radius r_{cham} (μm)	15
Filtration channel length L (μm)	15
Chamber length L_{cham} (μm)	30
Surface tension σ (mN/m)	50
Blood viscosity μ_f (Pa·s)	0.001
Cell viscosity μ_{cell} (Pa·s)	0.001–0.064
Viscosity ratio λ (μ_{cell}/μ_f)	1–64
Wall contact angle θ	180

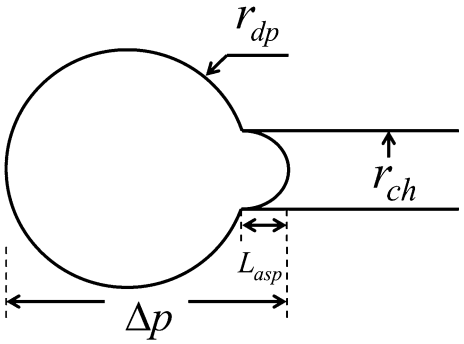

Fig. 2 Initial stage of a cell squeezing into a microfilter

acceleration vector, and $\vec{F}$ represents the source term such as the interfacial forces.

When a viscous cell is squeezed through the filtration channel, the inlet pressure needed for the cell to pass through the filter channel can be expressed as:

$$P_{\text{inlet}} = P_{\text{surface}} + P_{\text{viscous}} \tag{2}$$

in which P_{surface} is the pressure drop due to surface tension and P_{viscous} is the pressure drop due to viscous resistance in the microfilter. For cylindrical filter channels, P_{surface} can be evaluated by using the following Young–Laplace equation:

$$\Delta p = \sigma\left(\frac{1}{R_1} + \frac{1}{R_2}\right), \tag{3}$$

where σ is the surface tension, R_1 and R_2 are the principal radii of the interface curvature, as shown in Fig. 2.

The viscous pressure drop P_{viscous} can be further expressed as,

$$P_{\text{viscous}} = P_{\text{vis\_major}} + P_{\text{vis\_minor}} \tag{4}$$

in which $P_{\text{vis\_major}}$ is the viscous pressure drop in the filtering channel, and $P_{\text{vis\_minor}}$ is the pressure loss due to sudden contraction and expansion in the filtering chamber. The minor pressure loss can be calculated by

$$P_{\text{vis\_minor}} = K_c\frac{\rho V^2}{2} + K_e\frac{\rho V^2}{2}, \tag{5}$$

where ρ is the density, V is the local flow velocity, and K_c and K_e are the pressure loss coefficients. K_c and K_e are set as 0.5 and 1, respectively, assuming that the filtering channel is much smaller than the filtering chambers.

4 Numerical method

For this study, the viscous cancer cell and the blood plasma establish a two-phase flow. The phases are treated as non-interpenetrating continua, and the cell membrane is represented by the interface between the two phases. To track the interface, various methods are available, including level set (Osher and Sethian 1988), front tracking (Unverdi and Tryggvason 1992), and volume-of-fluid (VOF) methods. In this paper, the VOF model is employed as it conserves mass well without having logic problems related to intersecting surfaces (Hirt and Nichols 1981). The VOF model first introduces a volume fraction value, α_k, for each cell of the computational grid (the subscript k denotes the kth fluid or phase). α_k has different values depending on the different grid cell conditions: When a grid cell is filled with the kth fluid, $\alpha_k = 1$; when a grid cell does not contain the kth fluid, $\alpha_k = 0$; when a grid cell contains both fluids, i.e., when there is an interface between the two phases, $0 < \alpha_k < 1$.

The interface can be tracked by solving the continuity equation of different phases. For the kth fluid, the equation is given by

$$\frac{\partial}{\partial t}(\alpha_k\rho_k) + \nabla\cdot(\alpha_k\rho_k\vec{u}_k) = S_k + \sum_{l=1}^{n}(\dot{m}_{lk} - \dot{m}_{kl}), \tag{6}$$

where ρ_k denotes the density of the kth fluid; $\vec{u}_k$ denotes the velocity; S_k denotes the mass source term which is zero in this problem; $\dot{m}_{lk}$ denotes the mass transfer from the lth to the kth fluid, and $\dot{m}_{kl}$ denotes the mass transfer from the kth to the lth fluid. For this study, the fluid is incompressible and there is no mass transfer between different phases. Each fluid property (e.g., density and viscosity) of the multiphase system is calculated by taking a volume fraction average of all fluids in a grid cell. Interpolation near the interface is achieved by employing the geometric reconstruction scheme.

The surface tension that acts in the cell membrane is modeled by the continuum-surface-force (CSF) method (Brackbill et al. 1992), which can accurately evaluate the surface tension effects without imposing restrictions on modeling the dynamic evolution of the cell–blood interface. In the CSF method, the surface curvature is computed from the local gradient of the interface normal vector $\vec{n}$, which is

defined as the gradient of the volume fraction of the kth fluid, i.e., $\vec{n} = \nabla\alpha_k$. The local curvature is defined as the divergence of the unit normal vector to the interface, i.e., $\kappa = \nabla \cdot \frac{\vec{n}}{|\vec{n}|}$. According to the divergence theorem, the interfacial force due to surface tension can be expressed as (Fluent 2011)

$$F_{\text{interfacial}} = \sum_{i<j} \sigma_{ij} \frac{\alpha_i \rho_i \kappa_j \nabla\alpha_j + \alpha_j \rho_j \kappa_i \nabla\alpha_i}{\frac{1}{2}(\rho_i + \rho_j)} \tag{7}$$

where ρ is the fluid density and σ_{ij} is the surface tension. This interfacial force can be added to the momentum equation as a source term.

Due to symmetry, 2-D axisymmetric analysis is employed in the study. A grid-independent study is first carried out in our study to ensure that the numerical solutions do not depend on the mesh density. As a result of such study, a fine uniform mesh throughout the computational domain is used in our numerical simulation to study the complex cell-channel–blood interactions in the CTC filter. The employment of the fine quadratic Cartesian mesh ensures the accuracy of the flow field results by virtue of its high precision and good convergence performance. The mesh has 384,000 grid cells generated for the computational domain with 42,000 grid cells patched for the viscous cell, as shown in Fig. 3.

Temporal terms of the governing equations are discretized by the second-order implicit differencing scheme. The momentum equation is discretized by the second-order upwind scheme, and pressure is discretized by the PRESTO method. The pressure–velocity coupling is calculated by the SIMPLE algorithm. Boundary conditions are set as follows: Velocity inlet at the entrance with the velocity U is set as 0.02 m/s, nonslip boundary for the microfilter walls, and pressure outlet at the exit. The ambient reference pressure is set as zero. Axisymmetric condition is imposed on the centerline of the microfilter. A multicore-based parallel processing is employed for computational speedup, and it takes about 384 CPU hours for each simulation case.

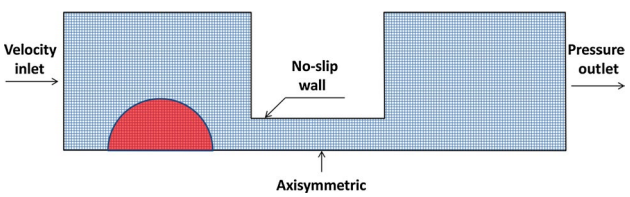

Fig. 3 Computation domain and mesh

5 Results and discussion

5.1 Pressure signature and cell viscosity

In cell-deformation-based CTC microfiltration devices, the blood sample with highly viscous CTCs is driven by the operating pressure (i.e., the inlet pressure) of the filtration system. The pressure characteristics during squeezing of the highly viscous cell play a key role in the normal operation of the microfiltration system. In this section, pressure characteristics of the CTC filtration process as well as the effects of varied cell viscosities are discussed in great detail. The inlet pressure variation with respect to time is hereby defined as the "pressure signature," which shows the important pressure characteristics and is presented in Fig. 4.

The pressure signature for squeezing a low-viscosity cell is compared with that for a high-viscosity cell as shown in Fig. 4. To better understand the pressure signatures, the deformed cell shape during the squeezing process is also plotted. For the low-viscosity case in Fig. 4a, the pressure profile is nearly antisymmetric due to an ideal surface tension dominant squeezing process. The surface-tension-induced pressures are 13.8 and −12.3 kPa, respectively, for entering (Fig. 4a-II) and exit stages (Fig. 4a-IV). These pressure values are very close to 12.5 kPa predicted from the classical Young–Laplace theorem [Eq. (3)].

In comparison, for highly viscous case in Fig. 4b, although one can see similar cell deformations and initial pressure peaks caused by surface tension, the pressure signature during the passing stage (Fig. 4b-III) differs significantly from that of the low-viscosity case in Fig. 4a-III. As shown in Fig. 4b, the pressure increases to a very high level when the viscous cell starts to fill up the filter. The passing of the viscous cell through the channel generates a second pressure peak with notable local fluctuations. It is interesting to notice from the magnified figure of Fig. 4b-III that a lubrication film of the blood plasma is formed between the highly viscous cell and channel wall, which is absent for the case of low viscosity. The lubrication film is identified as the main factor to the significant pressure increase during the cell passing stage (Fig. 4b-III).

The relationship between the maximum pressure (i.e., the maximum pressure drop in the channel) caused by the thin film and cell-to-blood viscosity ratio is plotted in Fig. 5. Note that the inlet pressure during a CTC passing event through a channel equals to the pressure drop in the channel, since the ambient reference pressure is set as zero as mentioned earlier. It is clear that the maximum pressure drop is affected by the cell viscosity significantly. Firstly, the maximum pressure drop maintains a lower value at very low-viscosity ratio ($\lambda = 1$). Then, the maximum pressure drop rises to very high values with the increased viscosity ratios ($4 < \lambda < 24$). Next, there is a

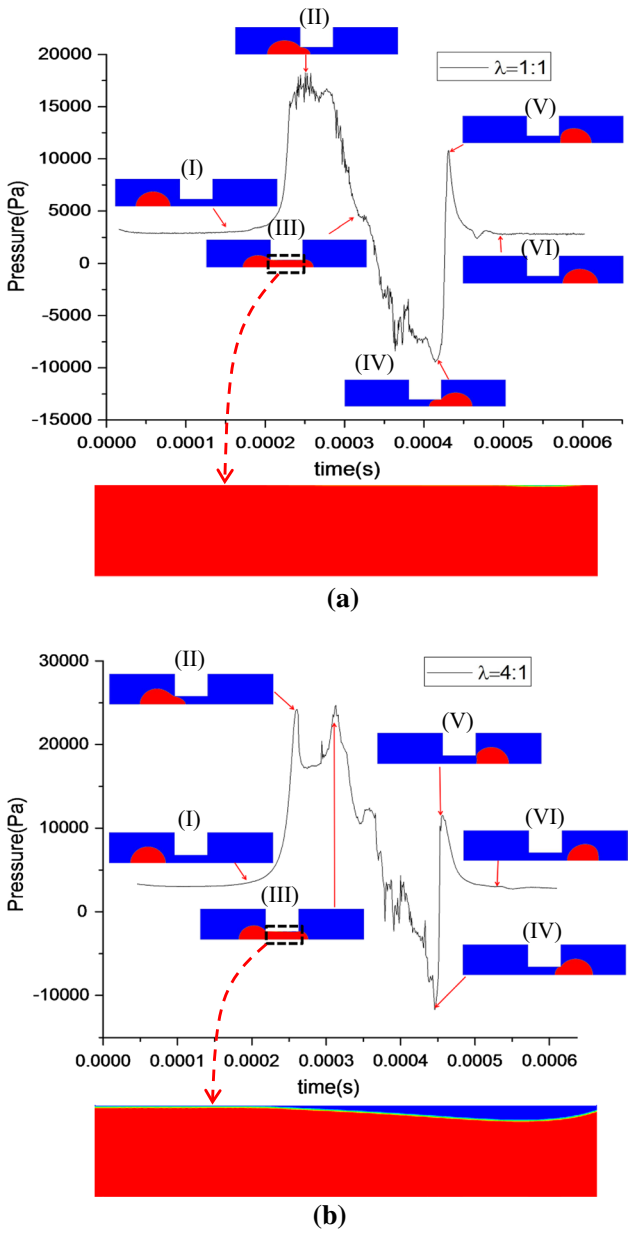

Fig. 4 Cell deformation with pressure history during the passing-through process: **a** $\lambda = 1{:}1$, **b** $\lambda = 4{:}1$

sharp decrease in the maximum pressure drop as the cell viscosity increases to larger values ($24 < \lambda < 40$). As cell viscosity further increases ($\lambda > 40$), the maximum pressure drop slightly grows with the cell viscosity. In fact, the variation of pressure drop is closely related to the thin film. The formation and topology of the film directly affect the local flow field, which in turn determines the local shear stress as well as the pressure drop. The pressure drop in turn determines the squeezing pressure of the cell. Therefore, the hydrodynamics of the thin film formed during the cell squeezing process needs to be thoroughly analyzed

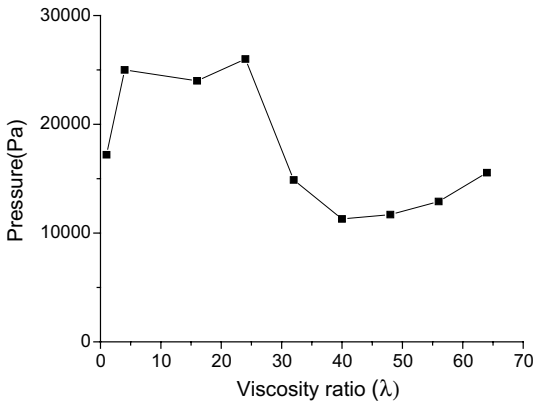

Fig. 5 Maximum pressure drop at different viscosity ratios

and characterized due to its significant effects on the cell squeezing pressure.

5.2 Hydrodynamics of the thin film formed in microfiltration

To study the passing event of the highly viscous cell, the thin-film lubrication squeezing process is modeled as an annular two-phase concurrent flow (Brenner 2013) as shown in Fig. 6. A coordinate system is defined for convenience of analysis. As shown in Fig. 6, the origin of the coordinate system is set at the intersection of the channel inlet and the axis of symmetry of the channel, with the positive x-axis pointing toward the flow direction.

During the passing process, there is a concurrent flow of viscous cell and blood plasma in the filter channel. The deformed viscous cell occupies the inner part of the filter channel when surrounded by an outer layer of the thin film of blood plasma. In this study, the two parts are

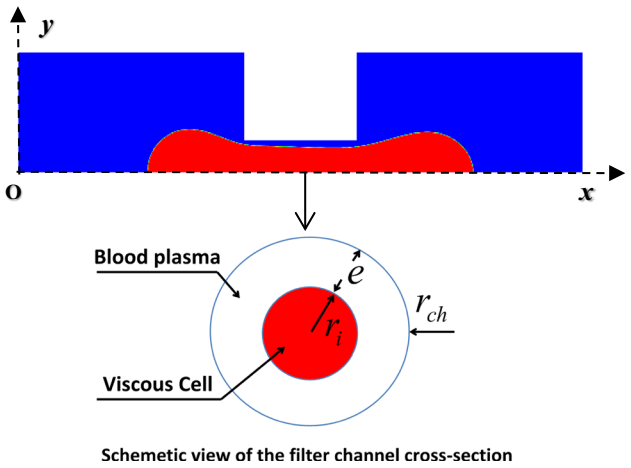

Fig. 6 Passing-through process and concurrent flow on the cross section

assumed to be radial-symmetric two-phase channel flow due to their identical densities (Brenner 2013, as shown in Fig. 6). Thus, the interface can be assumed to be circular with a radius of $r_i = r_{ch} - e$, where e is thickness of the film between the interface and the channel wall. The dynamic viscosities of the blood and cell are μ_f and μ_{cell}, respectively. The viscosity ratio is defined as $\lambda = \mu_{cell}/\mu_f$. The wall shear stress is denoted as τ_w.

For an annular two-phase concurrent flow, the velocity distribution in the center part (cell) is expressed as,

$$u_{cell} = \frac{\tau_w}{2\mu_{cell}} \cdot \left[\frac{\lambda \cdot (r_{ch}^2 - (r-e)^2) + ((r-e)^2 - r^2)}{r_{ch}} \right] \quad (8)$$

The velocity distribution in the gap (blood plasma) can be calculated by,

$$u_f = \frac{\tau_w}{2\mu_f} \cdot \left(\frac{r_{ch}^2 - r^2}{r_{ch}} \right) \quad (9)$$

where r is the radial location in the filter channel, and τ_w is the wall shear stress. Specifically, as the viscosity ratio is 1, the flow in the filter channel becomes a classic channel flow with parabolic profile. The wall shear stress τ_w can be determined based on the conservation of the volume flow rate $Q = Q_{chamber} = Q_{filter}$, where $Q_{chamber} = \pi r_{cham}^2 U$ is the volume flow rate at the chamber inlet, and Q_{filter} is the volume flow rate at the filter channel which can be calculated by velocity profile integration on the cross section

$$Q_{filter} = \int_0^{r_i} 2\pi r \cdot \mu_{cell} dr + \int_{r_i}^{r_{ch}} 2\pi r \cdot \mu_f dr \quad (10)$$

Finally, one can get τ_w which can be expressed as

$$\tau_w = \frac{4\mu_f r_{cham}^2 r_{ch} U}{r_{ch}^4 + \left(\frac{1}{\lambda} - 1\right) r_i^4} \quad (11)$$

Once the wall shear stress is determined in Eq. (11), one can obtain the velocity distribution as well as the pressure drop in the filter channel.

5.3 Cell viscosity effects on the thin film

As one can see in Eqs. (8) and (11), the thin film is a key factor for calculation of important flow properties (e.g., the velocity, shear rate, and shear stress distribution) in the filter channel during the squeezing process. The topologies of deformed cell and thin blood film at different viscosity ratios are given in Fig. 7. Since cells are usually highly viscous, this paper mainly focuses on highly viscous cases ($\lambda > 4$), i.e., the cell viscosity is at least a few times higher than the blood plasma. These cases have low capillary numbers Ca ($Ca = \frac{\mu U_l}{\sigma}$, where μ is the cell viscosity, U_l is the local velocity of the cell in the filter channel, and σ is the surface tension of the interface) within the range of 0.02–0.4.

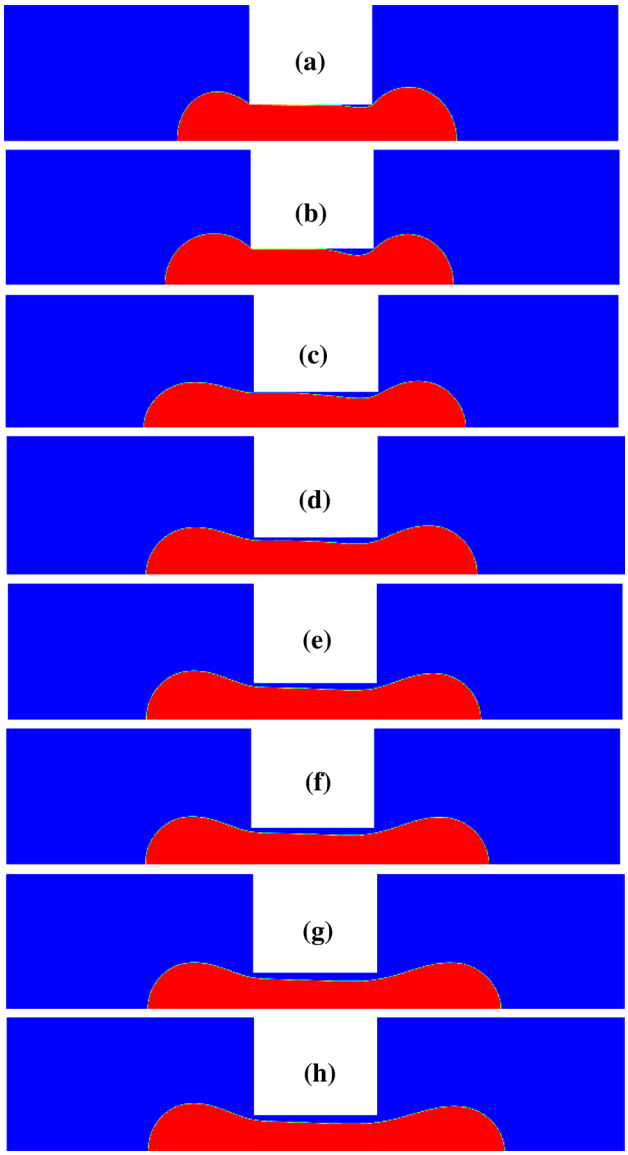

Fig. 7 Lubrication film evolution during the passing-through process: **a** λ = 4:1, **b** λ = 16:1, **c** λ = 24:1, **d** λ = 32:1, **e** λ = 40:1, **f** λ = 48:1, **g** λ = 56:1, **h** λ = 64:1

It is clear from Fig. 7a–c that the thin film of blood plasma gradually becomes thicker with the increase in cell viscosity. The film is located between the viscous cell and channel wall near the filtration channel exit and connects the passed and non-passed part of the cell. The constricted neck of the cell near the channel exit is mainly due to the increased cell viscosity, since the larger cell viscosity contributes to the cell stretching and balances

with the surface tension, as indicated by the capillary number.

When the viscosity ratio increases further, the viscous force contributes more to the stretching of the cell, and hence, the gap extends into a thin film all through the filter channel, as shown in Fig. 7d–f. When the cell viscosity increases to the highest values of current simulations, the viscous cell is further stretched and the extended gap between the channel wall and cell tends to develop into a uniform film with constant thickness all across the filter channel, as shown in Fig. 7g, h.

For all the passing-through process in Fig. 7a–h, the capillary force pushes the cell to deform against the channel wall and expels the blood plasma from the thin film into the bulk, while the viscous shear stress resists to the cell deforming. Thus, the film thickness is determined by the competition between the viscous shear stress and capillary force, which can be represented by the capillary number Ca. Due to the combined effects of viscosity and surface tension, one can see a monotonic increase in the thin-film thickness when the viscosity ratio increases, as shown in Fig. 7a–h.

To quantitatively characterize the lubrication film, Bretherton (1961) proposed a scaling law of the film thickness e in the case of inviscid bubble, moving in a circular tube with radius R

$$e/R \propto Ca^{2/3} \tag{12}$$

Hodges et al. (2004) analytically showed that Bretherton's scaling law is also appropriate for viscous drops and derived similar scaling law for viscous drops, which has a coefficient weakly depending on the viscosity ratio and the capillary number

$$\varepsilon = e/R = F(\lambda, Ca) \cdot Ca^{2/3} \tag{13}$$

where ε is the non-dimensional film thickness, and F is the coefficient determined by viscosity ratio and capillary number. These theoretical researches have been validated by both experiments (Schwartz et al. 1986) and numerical simulations (Reinelt and Saffman 1985).

As the thin-film thickness is not uniform in the filtration channel, it is calculated by taking the average value of the thin-film gap along the channel. The film thickness is non-dimensionalized based on the channel radius. The non-dimensional film thickness with respect to the non-dimensional capillary number is plotted in Fig. 8, and one can see the linear variation which consists with the theory. The coefficient F in Eq. (17) can be obtained ($F = 0.4223$) by the linear fit of the simulation data. Once the coefficient F is determined, Eq. (13) can quantitatively estimate the film thickness, which is required in Eqs. (8) and (11) for velocity and pressure drop characterization.

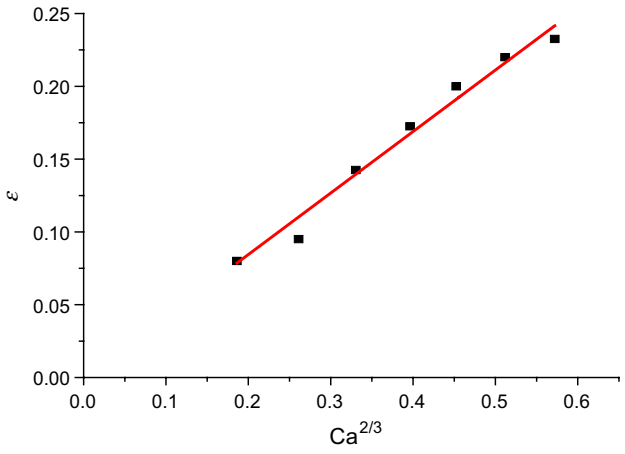

Fig. 8 Dimensionless film thickness between the viscous cell and channel wall

5.4 Cell viscosity effects on the flow velocity and pressure distribution

In this section, more detailed flow field properties regarding the thin film are presented. Figure 9 shows the velocity profiles across the filter channel at different viscosity ratios and different cross sections. Three cross sections located near the entry, midsection, and exit of the filtration channel (located at $x = 31$ μm, $x = 37.5$ μm, and $x = 44$ μm, respectively) are presented for comprehensive examination of the flow details throughout the filtration channel. Analytical results are also plotted in Fig. 9a for validation of the current simulation.

It is clear from Fig. 9a that, when the cell has identical viscosity with the blood plasma, the velocity in the filter channel is a parabolic profile that agrees well with analytical results. We notice that there are minor discrepancies between the two and local perturbations of the velocity profile near the interface. These perturbations are mainly due to the interactions between the cell and blood plasma. Such interactions are caused by the combined effects of surface tension and viscosity ratio.

As viscosity increases, the velocity profile is still a parabolic shape as shown in Fig. 9b. However, there are larger discrepancies between velocities at different cross sections. Also noticed are the increased shear rate and local perturbations near the interface and channel wall, due to increased cell viscosity effects. These velocity discrepancies and perturbations near the wall and interface have significant effects on the local pressure, since they can affect the local shear rate as well as shear stress which relates directly to the pressure drop in the filter channel.

As the local gap is enlarged and gets close to a thin-film shape (Fig. 7c, d) due to the increase in cell viscosity, the velocity profile in the channel begins to separate into two distinct parts: The part near the channel wall corresponds to

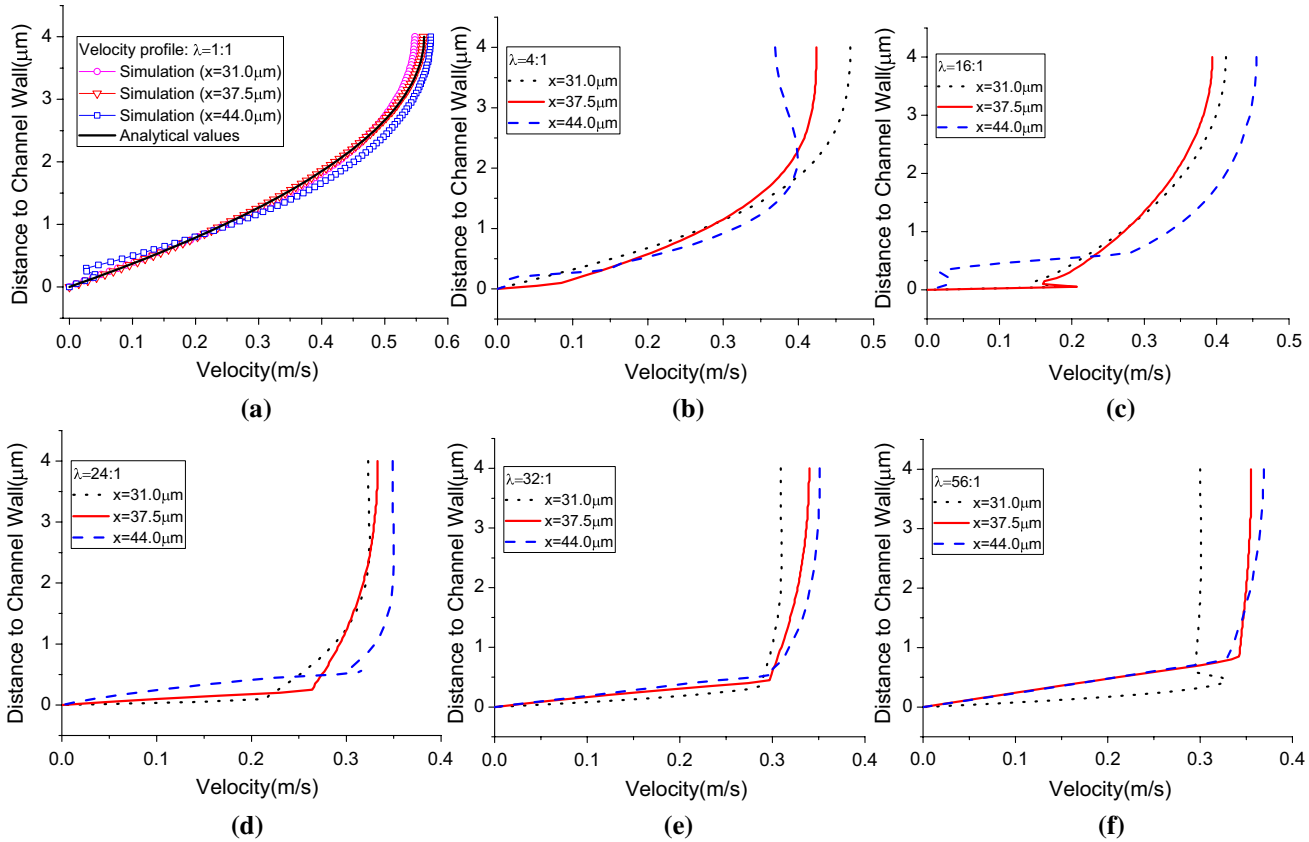

Fig. 9 Velocity in the filter channel: **a** $\lambda = 1{:}1$, **b** $\lambda = 4{:}1$, **c** $\lambda = 16{:}1$, **d** $\lambda = 24{:}1$, **e** $\lambda = 32{:}1$, **f** $\lambda = 56{:}1$

the annular film (as shown in Fig. 9c), and the other part near the centerline corresponds to the viscous cell in the channel center (as shown in Fig. 9d). In these cases of $\lambda \sim \varepsilon^{-1}$, as indicated by Jensen et al. (Hodges et al. 2004), there exist non-trivial interactions between the cell and ambient blood plasma. Due to the non-negligible interactions, the velocity discrepancies and perturbations near the wall are increased with highly inconsistent shear rate compared to the case in Fig. 9a. Those drastic perturbations of the velocity profile can result in large oscillating shear stress, which in turn leads to the large pressure and fluctuations.

When the thin film is already well established with a uniform thickness at higher viscosity ratios (Fig. 7e–h), one can see well-established two distinct parts in the velocity profile in Fig. 9e, f. Each part at different cross sections has similar velocity distributions and lower shear rates, rather than highly scattered velocity profiles with remarkable oscillations (Fig. 9c, d). The decreased shear rates and velocity discrepancies can result in a reduced pressure.

In addition, one can see the notable local velocity oscillations and extreme values at the interface as shown in Fig. 9. These extreme values are mainly caused by the interactions between the viscous cell and blood plasma in the film. Although these local small peaks are innocuous to the global velocity distribution, they can reduce the local shear rate which directly affects the local shear stress and reduce it to a small value. The reduced shear stress can in turn affect the local pressure distribution in the filter channel.

Figure 10 gives the local pressure drop in the well-established thin film and shows the effects of the local extreme values on the pressure drop. As one can see in Fig. 10, the average of pressure drop in the thin film basically coincides with the values shown in Fig. 5. Notably, when approaching to the interface, the pressure drop diminishes into a small value. This implies a sharp decrease in shear stress near the interface, which can be explained by the effects of aforementioned local extreme values near the interface, as shown in Fig. 9. These characteristics provide us more details regarding flow properties and pressure distributions in the microfilter and offer helps in the pressure signature estimation.

5.5 Estimation of the pressure drop

From the findings and discussions in Sect. 5.4, one can assume that the pressure drop (also known as "pressure differential") in the filter channel is mainly dominated by the thin film. Thus, only the annular thin film is considered as the major contribution to the pressure drop in the filter

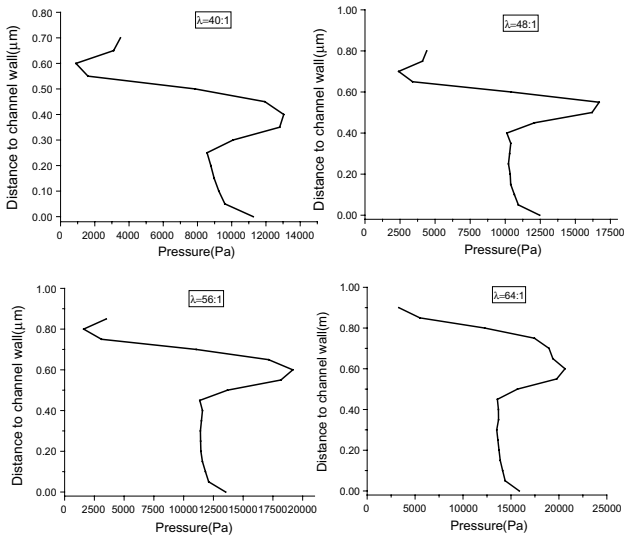

Fig. 10 Pressure drop distributions in the thin film of different cell viscosities

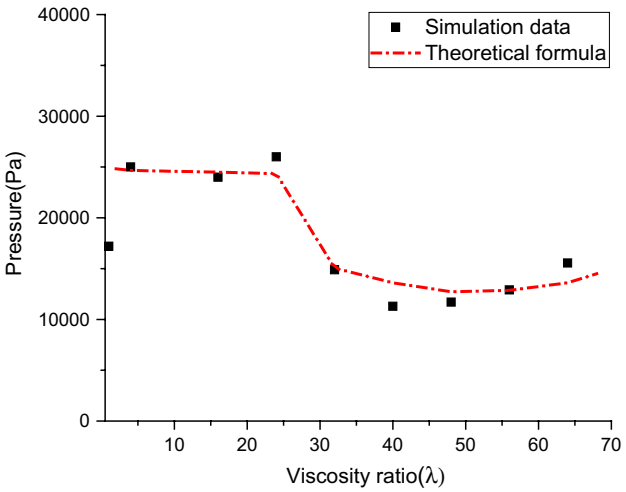

Fig. 11 Comparison of simulated and hypothetical results of the viscous pressure drop

channel. We propose an analytical method to estimate the pressure drop. The pressure drop expression is first derived by just considering the balance of shear stress and pressure in the filter channel. Then, the expression is adjusted with a term to include the effects of cell viscosity and the cell–blood interactions on pressure drop. The details of our derivation are found in "Appendix." Here, we obtain the pressure drop estimation formula as follows,

$$P = \frac{[1 + 2.67 \cdot Ca^{2/3} \ln(\lambda/\lambda_0)] \cdot 8\mu_f r_{cham}^2 LU}{\left[1 - (1 - 0.4223 \cdot Ca^{2/3})^2\right] \cdot \left[1 + \left(\frac{1}{\lambda} - 1\right) \cdot (1 - 0.4223 \cdot Ca^{2/3})^4\right] \cdot r_{ch}^4} \quad (14)$$

where Ca is the capillary number, λ is the viscosity ratio of viscous cell to blood plasma, μ_f is the viscosity of ambient blood plasma, L is the length of the filter channel, r_{cham} is the radius of the entrance and exit chamber, and r_{ch} is the filter channel radius. Equation (14) directly relates the pressure drop in the microfilter to the known system parameters (e.g., capillary number, geometric dimensions, inlet flow velocity, and viscosity ratio). Once the system parameters are given, the pressure drop can be quickly estimated using the proposed formula instead of running time-consuming CFD simulations.

Figure 11 shows the comparison of the pressure drop estimated from the proposed formula against predictions from simulation. A good match between them can be found in the high-cell-viscosity regions ($\lambda > 4$) in Fig. 11. Once the pressure drop is quantitatively determined, the threshold CTC passing pressure can be easily quantified by adding the pressure drop to the ambient working pressure of the CTC chip. Thus, the threshold passing pressure of the CTCs can be quickly obtained through the formula, which in turn facilitates and accelerates the CTC chip design and optimization process.

The application ranges of the formula for estimation of pressure drop during the squeezing process are summarized in Table 2. For low viscosities, the squeezing process can be fully characterized by Poiseuille and Young–Laplace equations. For highly viscous cells, the occupation stage [stage (III)] is dominated by the thin-film flow, and hence, the pressure drop needs to be estimated by our proposed method.

With the proposed formula, the whole squeezing process of high-viscous cells can be readily characterized. Due to its simplicity, the formula is useful for quick estimation and characterization of pressure signatures in cell-deformation-based cell microfiltration devices. The quick pressure characterization can in turn provide guidelines and speedup the design and optimization of such CTC chips.

In fact, besides CTC microfiltration devices, this formula can be applied to various microfluidic devices involving microscale capillary flows with highly viscous drops in microconfinements. For example, the microscale capillary flows are dominant in microchannel reactors with very-high-surface-to-volume ratios to intensify mass/heat transfer rates (Qian and Lawal 2006). Microchannels are also widely used in fuel combustion technology (Lin and Tavlarides 2009), physicochemical reaction processing and analysis (e.g., polymerase chain reaction (PCR); Walsh et al. 2006), and microfuel cells (Angeli and Gavriilidis 2008). By conducting numerical simulation and applying the proposed formula, one can have detailed understanding of the characteristics, such as flow field characters, mass or heat transfer, and the pressure drop, of microscale capillary flows in microconfinements and provide useful

Table 2 Squeezing stages and pressure characters

		Low-viscosity ratio ($\lambda \sim 1$)		High-viscosity ratio ($\lambda > 10$)	
		Pressure domination	Pressure drop calculation	Pressure domination	Pressure drop calculation
(I)	Entry	Poiseuille flow	$8\mu_f LQ/\pi r_{ch}^4$	Poiseuille flow	$8\mu_f LQ/\pi r_{ch}^4$
(II)	Squeezing-in	Surface tension	$\sigma(1/R_1 + 1/R_2)$	Surface tension	$\sigma(1/R_1 + 1/R_2)$
(III)	Cell occupation	Poiseuille flow	$8\mu_{cell} LQ/\pi r_{ch}^4$	Thin-film flow	Proposed formula (Eq. 18)
(IV)	Squeezing-out	Surface tension	$\sigma(1/R_1 + 1/R_2)$	Surface tension	$\sigma(1/R_1 + 1/R_2)$
(V)	Exit	Poiseuille flow	$8\mu_f LQ/\pi r_{ch}^4$	Poiseuille flow	$8\mu_f LQ/\pi r_{ch}^4$

guidelines to the design and optimization of such multiphase microdevices.

6 Conclusions

In this study, the behavior of circulating tumor cell during the microfiltration process is numerically investigated by using single droplet model encapsulated by a membrane with surface tension. The interface is tracked by VOF method and surface tension modeled by CSF model. Cell motion, deformation, and pressure signatures are discussed in great detail in this study. Also discussed are the effects of viscosity ratio on the microfiltration process. Our numerical results and analysis provide insights into the physics behind the filtering process and provide useful guidance to the design and optimization of such devices as well. Important conclusions are drawn from the study:

Firstly, the current simulation based on highly viscous droplet model shows a good agreement with analytic results regarding the cell deformation as well as flow characteristics such as velocity distributions and pressure signatures. Secondly, cell viscosity is shown to have significant effects on the deformability-based CTC separation process. CTCs with very high viscosity lead to a thin-film-dominated flow in the filtration channel during the squeezing process. The thin film formed between the viscous cell and channel wall dominates the flow characteristics such as shear stress and pressure distribution in the filtration channel. Thirdly, a theoretical formula is proposed to estimate the pressure drop for highly viscous CTC separation process. The proposed formula is useful for quick estimation and characterization of the pressure signatures during the microfiltration process.

Appendix: derivation of pressure drop estimating formula

For calculation of the pressure drop in the filter channel, the balance of the fluids in the filter channel is expressed as

$$F_i - F_o = P * A = 2\pi r_{ch} L \tau_w \tag{15}$$

in which F_i and F_o are the forces imposed on the cross sections of filter channel inlet and outlet, respectively; A is the effective area where the main pressure drop is imposed. According to the pressure distribution in the filter channel, the pressure is mainly imposed on the annular film which has the area $A = \pi(r_{ch}^2 - r_i^2)$. Based on Eq. (15) and the hydrodynamic theory of the thin film Eq. (11), the theoretical pressure is expressed as

$$P_{theoretical} = \frac{8\mu_f r_{cham}^2 r_{ch}^2 LU}{\left(r_{ch}^2 - r_i^2\right) \cdot \left(r_{ch}^4 + \left(\frac{1}{\lambda} - 1\right) r_i^4\right)} \tag{16}$$

To consider the effects of deformation resistance and the interactions on the interface, a correction term P' needs to be added to the theoretical value

$$P = P_{theoretical} + P' \tag{17}$$

P' is the correction term expressed as $P' = K \cdot P_{theoretical}$, in which K is a coefficient determined by viscosity ratio and film thickness. Considering the contribution of both shear stress and the cell resistance to deformation, the annular film and viscosity are the major factors affecting the viscous pressure. We propose that the coefficient adheres to the simple form,

$$K = K(\varepsilon, \lambda) = k \cdot \varepsilon \cdot f(\lambda) \tag{18}$$

In which k is a constant, ε is the non-dimensional film thickness, and $f(\lambda)$ is a function of viscosity ratio. Considering the variable combined effects introduced by different viscosity ratio values, $f(\lambda)$ is assigned the form $f(\lambda) = \ln(\lambda/\lambda_0)$, where λ is the viscosity ratio and λ_0 corresponds to the case when viscous resistance balances with carrier–drop interactions, and pressure drop reaches the minimum level, with the λ_0 value ($\lambda_0 = 36$) being obtained from simulation data. Based on Eq. (13), one can get the non-dimensional thin-film thickness expressed as

$$\varepsilon = e/r_{ch} = 0.4223 \cdot Ca^{2/3} \tag{19}$$

By applying least-square method to the simulation data, one can get the optimum value of $k = 6.32$. Thus, the formula for viscous pressure correction term is finally expressed as

$$P' = 2.67 \cdot Ca^{2/3} \ln(\lambda/\lambda_0) \cdot P_{\text{theoretical}} \tag{20}$$

Then, the pressure drop is expressed as

$$P = [1 + 2.67 \cdot Ca^{2/3} \ln(\lambda/\lambda_0)] \cdot P_{\text{theoretical}} \tag{21}$$

With Eqs. (16) and (21) can be rewritten as,

$$P = \frac{[1 + 2.67 \cdot Ca^{2/3} \ln(\lambda/\lambda_0)] \cdot 8\mu_f r_{\text{cham}}^2 r_{\text{ch}}^2 LU}{\left(r_{\text{ch}}^2 - r_i^2\right) \cdot \left(r_{\text{ch}}^4 + \left(\frac{1}{\lambda} - 1\right) r_i^4\right)} \tag{22}$$

Based on the definition of $r_i = r_{\text{ch}} - e$ and the film thickness $e = 0.4223 \cdot Ca^{2/3} \cdot r_{ch}$ [from Eq. (19)], Eq. (22) has the final form as,

$$P = \frac{[1 + 2.67 \cdot Ca^{2/3} \ln(\lambda/\lambda_0)] \cdot 8\mu_f r_{\text{cham}}^2 LU}{\left[1 - (1 - 0.4223 \cdot Ca^{2/3})^2\right] \cdot \left[1 + \left(\frac{1}{\lambda} - 1\right) \cdot (1 - 0.4223 \cdot Ca^{2/3})^4\right] \cdot r_{\text{ch}}^4} \tag{23}$$

References

Aghaamoo M, Zhang Z, Chen X, Xu J (2015) Deformability-based circulating tumor cell separation with conical-shaped microfilters: concept, optimization, and design criteria. Biomicrofluidics 9:034106

Allan AL, Keeney M (2009) Circulating tumor cell analysis: technical and statistical considerations for application to the clinic. J Oncol 2010. doi:10.1155/2010/426218

Angeli P, Gavriilidis A (2008) Hydrodynamics of Taylor flow in small channels: a review. Proc Inst Mech Eng C J Mech Eng Sci 222:737–751

Bhagat AAS, Hou HW, Li LD, Lim CT, Han J (2011) Pinched flow coupled shear-modulated inertial microfluidics for high-throughput rare blood cell separation. Lab Chip 11:1870–1878

Boey SK, Boal DH, Discher DE (1998) Simulations of the erythrocyte cytoskeleton at large deformation. I. Microsc Mod Biophys J 75:1573–1583

Bonner W, Hulett H, Sweet R, Herzenberg L (1972) Fluorescence activated cell sorting. Rev Sci Instrum 43:404–409

Brackbill J, Kothe DB, Zemach C (1992) A continuum method for modeling surface tension. J Comput Phys 100:335–354

Brenner H (2013) Viscous flows: the practical use of theory. Butterworth-Heinemann, Oxford

Bretherton F (1961) The motion of long bubbles in tubes. J Fluid Mech 10:166–188

Brody JP, Osborn TD, Forster FK, Yager P (1996) A planar microfabricated fluid filter. Sens Actuators A 54:704–708

Chen X, Liu CC, Li H (2008) Microfluidic chip for blood cell separation and collection based on crossflow filtration. Sens Actuators B Chem 130:216–221

Cima I, Yee CW, Iliescu FS, Phyo WM, Lim KH, Iliescu C, Tan MH (2013) Label-free isolation of circulating tumor cells in microfluidic devices: current research and perspectives. Biomicrofluidics 7:011810

Crowley TA, Pizziconi V (2005) Isolation of plasma from whole blood using planar microfilters for lab-on-a-chip applications. Lab Chip 5:922–929

Di Carlo D (2009) Inertial microfluidics. Lab Chip 9:3038–3046

Ding X et al (2013) Surface acoustic wave microfluidics. Lab Chip 13:3626–3649

Faivre M, Abkarian M, Bickraj K, Stone HA (2006) Geometrical focusing of cells in a microfluidic device: an approach to separate blood plasma. Biorheology 43:147–159

Fluent A (2011) Ansys fluent theory guide. ANSYS Inc, Canonsburg

Freund JB (2014) Numerical simulation of flowing blood cells. Annu Rev Fluid Mech 46:67–95

Fulwyler MJ (1965) Electronic separation of biological cells by volume. Science 150:910–911

Gascoyne PR, Noshari J, Anderson TJ, Becker FF (2009) Isolation of rare cells from cell mixtures by dielectrophoresis. Electrophoresis 30:1388–1398

Gossett DR et al (2010) Label-free cell separation and sorting in microfluidic systems. Anal Bioanal Chem 397:3249–3267

Guo Q, McFaul SM, Ma H (2011) Deterministic microfluidic ratchet based on the deformation of individual cells. Phys Rev E 83:051910

Gupta GP, Massagué J (2006) Cancer metastasis: building a framework. Cell 127:679–695

Hirt CW, Nichols BD (1981) Volume of fluid (VOF) method for the dynamics of free boundaries. J Comput Phys 39:201–225

Hodges S, Jensen O, Rallison J (2004) The motion of a viscous drop through a cylindrical tube. J Fluid Mech 501:279–301

Huang LR, Cox EC, Austin RH, Sturm JC (2004) Continuous particle separation through deterministic lateral displacement. Science 304:987–990

Hur SC, Henderson-MacLennan NK, McCabe ER, Di Carlo D (2011) Deformability-based cell classification and enrichment using inertial microfluidics. Lab Chip 11:912–920

Ji HM, Samper V, Chen Y, Heng CK, Lim TM, Yobas L (2008) Silicon-based microfilters for whole blood cell separation. Biomed Microdevice 10:251–257

Jin C, McFaul SM, Duffy SP, Deng X, Tavassoli P, Black PC, Ma H (2014) Technologies for label-free separation of circulating tumor cells: from historical foundations to recent developments. Lab Chip 14:32–44

Jönsson C et al (2008) Silane–dextran chemistry on lateral flow polymer chips for immunoassays. Lab Chip 8:1191–1197

Krebs MG, Hou J-M, Ward TH, Blackhall FH, Dive C (2010) Circulating tumour cells: their utility in cancer management and predicting outcomes. Ther Adv Med Oncol 2:351–365

Kumar A, Bhardwaj A (2008) Methods in cell separation for biomedical application: cryogels as a new tool. Biomed Mater 3:034008

Leong FY, Li Q, Lim CT, Chiam K-H (2011) Modeling cell entry into a micro-channel. Biomech Model Mechanobiol 10:755–766

Li J, Dao M, Lim C, Suresh S (2005) Spectrin-level modeling of the cytoskeleton and optical tweezers stretching of the erythrocyte. Biophys J 88:3707–3719

Lim C, Zhou E, Quek S (2006) Mechanical models for living cells—a review. J Biomech 39:195–216

Lin R, Tavlarides LL (2009) Flow patterns of n-hexadecane–CO 2 liquid–liquid two-phase flow in vertical pipes under high pressure. Int J Multiph Flow 35:566–579

Liu Z, Huang F, Du J, Shu W, Feng H, Xu X, Chen Y (2013) Rapid isolation of cancer cells using microfluidic deterministic lateral displacement structure. Biomicrofluidics 7:011801

Lu B, Xu T, Zheng S, Goldkorn A, Tai Y-C (2010) Parylene membrane slot filter for the capture, analysis and culture of viable circulating tumor cells. In: Micro Electro Mechanical Systems (MEMS), 2010 IEEE 23rd international conference, IEEE, pp 935–938

Luo Y et al (2014) A constriction channel based microfluidic system enabling continuous characterization of cellular instantaneous Young's modulus. Sens Actuators B Chem 202:1183–1189

Marella SV, Udaykumar H (2004) Computational analysis of the deformability of leukocytes modeled with viscous and elastic structural components. Phys Fluids (1994-present) 16:244–264
McFaul SM, Lin BK, Ma H (2012) Cell separation based on size and deformability using microfluidic funnel ratchets. Lab Chip 12:2369–2376
Melville D, Paul F, Roath S (1975) Direct magnetic separation of red cells from whole blood. Nature 255:706. doi:10.1038/255706a0
Miltenyi S, Müller W, Weichel W, Radbruch A (1990) High gradient magnetic cell separation with MACS. Cytometry 11:231–238
Mohamed H, Turner JN, Caggana M (2007) Biochip for separating fetal cells from maternal circulation. J Chromatogr A 1162:187–192
Mohamed H, Murray M, Turner JN, Caggana M (2009) Isolation of tumor cells using size and deformation. J Chromatogr A 1216:8289–8295
Münz M et al (2010) Side-by-side analysis of five clinically tested anti-EpCAM monoclonal antibodies. Cancer Cell Int 10:1
Nie Z et al (2008) Emulsification in a microfluidic flow-focusing device: effect of the viscosities of the liquids. Microfluid Nanofluid 5:585–594
Osher S, Sethian JA (1988) Fronts propagating with curvature-dependent speed: algorithms based on Hamilton-Jacobi formulations. J Comput Phys 79:12–49
Peng Z, Li X, Pivkin IV, Dao M, Karniadakis GE, Suresh S (2013) Lipid bilayer and cytoskeletal interactions in a red blood cell. Proc Natl Acad Sci 110:13356–13361
Polyak K, Weinberg RA (2009) Transitions between epithelial and mesenchymal states: acquisition of malignant and stem cell traits. Nat Rev Cancer 9:265–273
Preetha A, Huilgol N, Banerjee R (2005) Interfacial properties as biophysical markers of cervical cancer. Biomed Pharmacother 59:491–497
Qian D, Lawal A (2006) Numerical study on gas and liquid slugs for Taylor flow in a T-junction microchannel. Chem Eng Sci 61:7609–7625
Reinelt D, Saffman P (1985) The penetration of a finger into a viscous fluid in a channel and tube. SIAM J Sci Stat Comput 6:542–561
Ren L et al (2015) A high-throughput acoustic cell sorter. Lab Chip 15:3870–3879
Schwartz L, Princen H, Kiss A (1986) On the motion of bubbles in capillary tubes. J Fluid Mech 172:259–275
Seal S (1964) A sieve for the isolation of cancer cells and other large cells from the blood. Cancer 17:637–642
Secomb TW, Hsu R (1996) Analysis of red blood cell motion through cylindrical micropores: effects of cell properties. Biophys J 71:1095
Shelby JP, Mutch SA, Chiu DT (2004) Direct manipulation and observation of the rotational motion of single optically trapped microparticles and biological cells in microvortices. Anal Chem 76:2492–2497
Sieuwerts AM et al (2009) Anti-epithelial cell adhesion molecule antibodies and the detection of circulating normal-like breast tumor cells. J Natl Cancer Inst 101:61–66
Tang Y, Shi J, Li S, Wang L, Cayre YE, Chen Y (2014) Microfluidic device with integrated microfilter of conical-shaped holes for high efficiency and high purity capture of circulating tumor cells. Sci Rep 4:6052
Torre LA, Bray F, Siegel RL, Ferlay J, Lortet-Tieulent J, Jemal A (2015) Global cancer statistics, 2012. CA Cancer J Clin 65:87–108
Unverdi SO, Tryggvason G (1992) A front-tracking method for viscous, incompressible, multi-fluid flows. J Comput Phys 100:25–37
VanDelinder V, Groisman A (2006) Separation of plasma from whole human blood in a continuous cross-flow in a molded microfluidic device. Anal Chem 78:3765–3771
Walsh E, King C, Grimes R, Gonzalez A (2006) Influence of segmenting fluids on efficiency, crossing point and fluorescence level in real time quantitative PCR. Biomed Microdevice 8:59–64
Warkiani ME, Khoo BL, Wu L, Tay AKP, Bhagat AAS, Han J, Lim CT (2016) Ultra-fast, label-free isolation of circulating tumor cells from blood using spiral microfluidics. Nat Protoc 11:134–148
Weigelt B, Peterse JL, Van't Veer LJ (2005) Breast cancer metastasis: markers and models. Nat Rev Cancer 5:591–602
Whitesides GM (2006) The origins and the future of microfluidics. Nature 442:368–373
Xiong W, Zhang J (2012) Two-dimensional lattice Boltzmann study of red blood cell motion through microvascular bifurcation: cell deformability and suspending viscosity effects. Biomech Model Mechanobiol 11:575–583
Zhang Z, Xu J, Chen X (2014a) Modeling cell deformation in CTC microfluidic filters. In: ASME 2014 international mechanical engineering congress and exposition. American Society of Mechanical Engineers, pp V003T003A034–V003T003A034
Zhang Z, Xu J, Chen X (2014b) Predictive model for the cell passing pressure in deformation-based CTC chips. In: ASME 2014 international mechanical engineering congress and exposition. American Society of Mechanical Engineers, pp V010T013A043–V010T013A043
Zhang Z, Xu J, Hong B, Chen X (2014c) The effects of 3D channel geometry on CTC passing pressure–towards deformability-based cancer cell separation. Lab Chip 14:2576–2584
Zhang Z, Chen X, Xu J (2015a) Entry effects of droplet in a micro confinement: Implications for deformation-based circulating tumor cell microfiltration. Biomicrofluidics 9:024108
Zhang Z, Xu J, Chen X (2015b) Compound droplet modelling of circulating tumor cell microfiltration. In: ASME 2015 international mechanical engineering congress and exposition. American Society of Mechanical Engineers, pp V07BT09A008–V007BT009A008
Zheng S, Lin H, Liu J-Q, Balic M, Datar R, Cote RJ, Tai Y-C (2007) Membrane microfilter device for selective capture, electrolysis and genomic analysis of human circulating tumor cells. J Chromatogr A 1162:154–161
Zheng S, Lin HK, Lu B, Williams A, Datar R, Cote RJ, Tai Y-C (2011) 3D microfilter device for viable circulating tumor cell (CTC) enrichment from blood. Biomed Microdevice 13:203–213